Editors' Suggestion

# Correlating dynamic microstructure to observed color in electrophoretic displays via *in situ* small-angle x-ray scattering

Scott C. Bukosky,[1,2] Joshua A. Hammons,[1] Brian Giera,[1] Elaine Lee,[1] Jinkyu Han,[1] Megan C. Freyman,[1] Anna Ivanovskaya,[1] Kerry G. Krauter,[1] Joshua D. Kuntz,[1] Marcus A. Worsley,[1] T. Yong-Jin Han,[1] William D. Ristenpart,[2] and Andrew J. Pascall[1,*]

[1]*Lawrence Livermore National Laboratory, Livermore, California 94551, USA*

[2]*Department of Chemical Engineering, University of California Davis, Davis, California 95616, USA*

(Received 9 March 2019; revised 4 May 2020; accepted 16 June 2020; published 27 July 2020)

Electrophoretic deposition (EPD) is an industrially relevant and scalable technique used to form particle deposits from colloidal suspensions. Highly concentrated particle suspensions generally prevent real-time *in situ* microscopy observations which limit the characterization of EPD films to *ex situ*, or postprocessed, laboratory techniques. For dynamic systems, such as tunable amorphous photonic crystals (APCs), only reversible deposits are formed during the EPD process. Since reversible deposits cannot be characterized with standard *ex situ* methods, the particle-particle and particle-field interactions that govern the displayed color and crystallinity of these systems are not well understood. Here, we present *in situ* small-angle x-ray scattering and UV-Vis techniques for measuring both the structural and optical response of an APC under applied electric fields. We also develop a computational model based on colloidal interactions to explain the observed change in the interparticle spacing of APCs due to the applied electric field which correlates to displayed color. Ultimately, this work provides a new *in situ* characterization method that could be expanded for other dynamic, tunable colloidal systems.

DOI: 10.1103/PhysRevMaterials.4.075802

## I. INTRODUCTION

Electrophoretic deposition (EPD) has been widely studied both experimentally [1,2] and theoretically [1,3–5] as a technique for the assembly and formation of colloidal deposits via the application of an external electric field. Due to its versatility, EPD is commonly used to form stable films from particle suspensions for a wide variety of applications such as high strength and/or functionally graded ceramics [1,6–10], energetic thin films [11], catalytic membranes [12] and solid oxide fuel cells [13], phosphorescent films [14], graphene based devices [15], and biomaterials and coatings [8,16]. EPD experiments are typically performed at particle volume fractions of a few percent where suspensions can be optically opaque. *In situ* particle level observations using standard optical or confocal microscopy techniques are, therefore, not possible. Instead, characterizations of colloidal systems are generally done purely *ex situ* by either weighing the deposited film or by using traditional 2D laboratory-based methods such as scanning/transmission electron microscopy (SEM/TEM) [2,16], and x-ray imaging techniques such as computed tomography [17,18]. These *ex situ* approaches, however, are performed after the deposit is formed and often require drying, cutting, or postprocessing of the sample, which can lead to restructuring or cracking of the film [2,7].

More advanced x-ray scattering techniques have also been used to characterize colloidal crystals [19–23]. In one such study, Krejci, *et al.* [22] were able to circumvent drying their samples by developing a solvent exchange technique to examine the as-made deposits. Since the samples were still characterized after the deposit was formed, no real-time, *in situ* information about the interparticle dynamics could be obtained. In an attempt to resolve these space and time dynamics, Yu *et al.* [24] recently performed a grazing-incidence small angle x-ray scattering (GISAXS) experiment to analyze nanocrystals deposited onto an electrode. Their system used low particle volume fractions ($< 0.1\%$) and was modeled as a suspension of simple spheres. In order to correlate the *in situ* particle dynamics and physics to the bulk physical properties of typical EPD systems, however, a sufficiently large number of particles ($>1\%$) are required and more complex particle morphologies must be considered.

For select applications, particularly electrophoretic displays and amorphous photonic crystals (APCs) [23,25–30], the applied electric field does not lead to the formation of a stable deposit. The displayed color of such devices is partially attributable to the underlying structure of deposit and is similar to how many organisms found in nature display color [19,21,28–31]. With this idea in mind, the devices can be systematically tuned by modulating the external field to induce a change in the interparticle spacing and structure of the deposit which results in a desired color response. Once the applied bias is removed, the particles resuspend and relax back to their initial state. While the color differences resulting from the applied potential can be quantitatively characterized by use of simple digital video analysis [32], the underlying structural rearrangement of the film that leads to these colors

*Corresponding author: pascall1@llnl.gov

 

cannot be determined by such analysis. Likewise, given the reversibility of these systems, the *ex situ* characterization techniques traditionally employed for measuring the crystallinity, morphology, and/or particle spacing of fixed films are not viable. In fact, changes in the average interparticle spacing of electrically tunable APCs are often indirectly calculated based on the wavelength at which maximum reflection occurs ($\lambda_{max}$). The volume-average center-to-center interparticle distance $\eta$ is then inferred from the mean particle correlation scattering for normal incident light:

$$m\lambda_{max} = 2\eta n_{eff}, \quad (1)$$

where $m$ is the order of reflection, $n_{eff}$ is the effective refractive index of the system and $\eta$ is necessarily assumed to be isotropic. Additional assumptions for tunable APC systems also typically include face-centered cubic (FCC) or other simple packing orders [27,30,31].

In order to avoid assumptions of the structure and morphology of the crystal, we present a direct measurement of $\eta$ obtained by small angle x-ray scattering (SAXS), which is often a nondestructive method that can be used to measure and resolve particle characteristics on length scales from less than 10 Å up to ∼15 $\mu$m [33]. Since x-ray scattering is very sensitive to order, no assumptions about the APC packing are required. From these transmission SAXS measurements, $\eta$ normal to the applied field is obtained by fitting the scattering data to an appropriate model and structure factor. The value of $\eta$ is used compute $\lambda_{max}$. This computed value is compared to that measured directly with ultraviolet-visible (UV-Vis) spectroscopy.

In addition to the direct SAXS measurements, we provide a computational model based on traditional colloidal Derjaguin-Landau-Verywey-Overbeek (DLVO) theory to confirm and predict changes in the interparticle spacing as a function of applied electric field. This technique provides a means to use a small-scale theoretical framework to provide insight into the overall time averaged dynamics of tunable, color changing photonic crystals.

## II. EXPERIMENTAL METHODS

### A. Sample cell preparation and characterization

The APC system consisted of hematite/silica ($Fe_2O_3/SiO_2$) core/shell particles (mean particle diameter, $\bar{D}_p = 155 \pm 2.0$ nm) that were prepared using a modified Stöber method and terminated with silanol end groups (cf. Han *et al.* [23] for a full description of the particle synthesis). These particles are negatively charged and have unique color properties that result from a balance between the inherent pigmentary color of hematite and the variations in structural color that arise from the short-range ordering of the particles. The strength of the applied electric field during EPD as well as the particle concentration control the interparticle separation and packing order (i.e., the perceived color of the APC).

The core/shell particles were suspended in propylene carbonate with concentrations ranging from 19–63 vol% [Fig. 1(c)], and electrophoretic light scattering (Malvern Zetasizer ZS90) was used to determine an electrophoretic mobility of $-0.6584 \pm 0.0309$ $\mu$m cm s$^{-1}$ V$^{-1}$. Sample cell fabrication and assembly were performed similar to previous work [23,34,35] where two parallel plate electrodes coated with indium-tin oxide (ITO, 13 $\Omega/sq$ measured, Sigma-Aldrich) are separated by a nonconductive spacer [Fig. 1(a)]. Here, the spacer thickness and separation distance between the electrodes was 20 $\mu$m, and approximately 8 $\mu$L of the particle suspension was used to fill the sample well. Once the device was sealed with the top electrode, a DC voltage was applied in incremental steps from 1 to 5 V. The field was then removed, and the device was allowed to gradually relax back to steady state; full relaxation typically took ∼1-2 minutes. For all experiments, video recordings were taken using a Canon EOS Rebel T6 digital camera. To establish a reference for the initial device color, video was started ∼1 minute prior to the application of the electric field. The observed color changes and reflectance spectra of the sample after the field was applied were measured using a UV-Vis spectrophotometer (Thorlabs CCS200) with a broad-spectrum LED light source (Thorlabs MCWHLP1 Mounted LED), and the DC voltage procedure described above was repeated with simultaneous UV-Vis measurements.

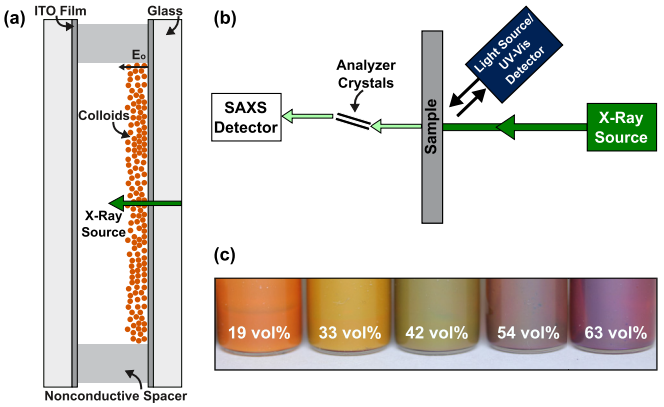


FIG. 1. (a) Schematic of a sample device depicting particle packing near the surface of the working electrode in response to an applied DC field. (b) Diagram of the *in situ* experimental setup during x-ray scattering measurements (diagrams are not to scale). (c) Representative images of bulk $Fe_2O_3/SiO_2$ core/shell particles suspended in propylene carbonate at varying concentration.

The electrochemical stability of ($Fe_2O_3/SiO_2$) core/shell particles suspended in propylene carbonate was also investigated using cyclic voltammetry with a potentiostat (Gamry Interface 1000E). After an equilibrium time of 5 seconds, cyclic voltammograms were measured from 0 to 5 V at a rate of 0.1 V/s and a step size of 2 mV. Impedance measurements were performed at 10 mV rms AC voltage from 1 MHz to 1 Hz and 10 points/decade. The resulting solution conductivity was calculated to be 14 $\mu$S/cm.

### B. Small-angle x-ray scattering data collection

The structure of the particles in suspension as well as their morphology was evaluated using the ultrasmall-angle x-ray scattering (USAXS) instrument [33] at Argonne National Laboratory's Advanced Photon Source, Sector 9-ID-C. Here, the scattered x-ray intensity was measured starting from ultra-low angles up to relatively large angles. A simplified schematic of the beamline setup is shown in Fig. 1(b). The Bonse-Hart instrument and sample geometry were chosen to

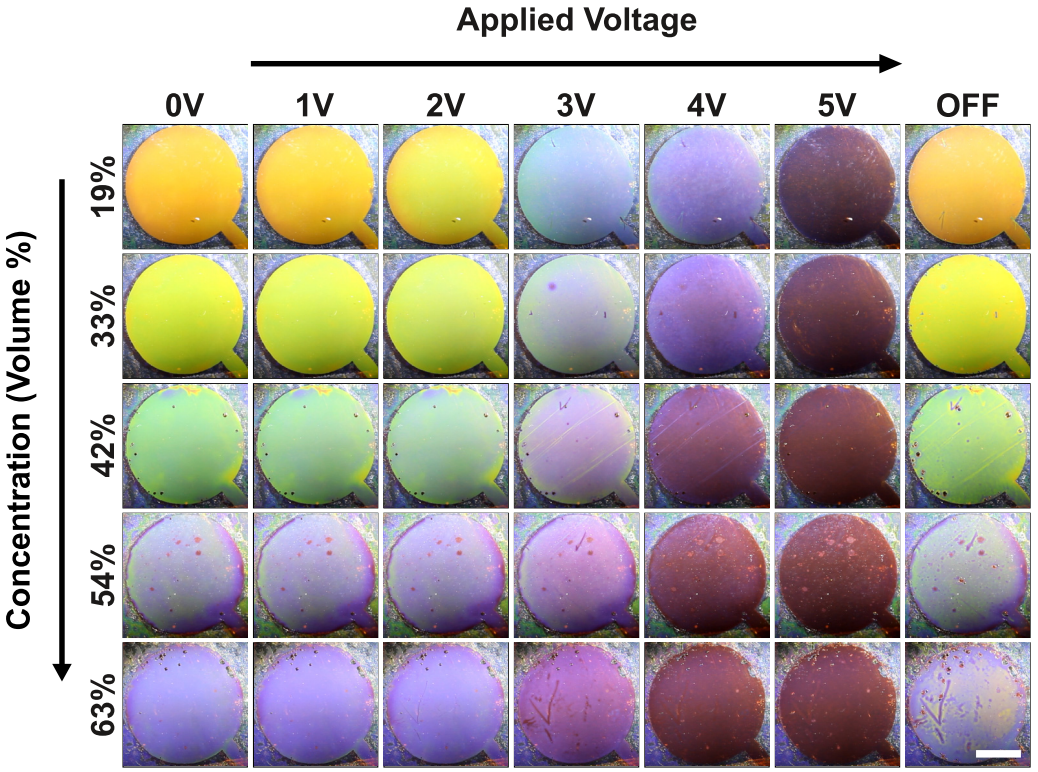


FIG. 2. Representative images of the observed structural color response as a function of voltage for each concentration of $Fe_2O_3/SiO_2$ particles. After applying 5 V, the field was removed (OFF), and the color was observed to approach its initial state. The scale bar is 5 mm.

(1) obtain the scattering from a large number of particles throughout the entire thickness of the sample cell by collecting USAXS data from a beam area that is larger than most pin-hole SAXS instruments and (2) ensure that the particle structure parallel to the substrate is measured so that slit smearing can be accounted for in the analysis. It should be noted that the scattering in the direction of the slit-length is also parallel to the surface. The scattered intensity collected at different angles provides information about both the structure and morphology of the particles and is commonly presented as the intensity vs. the magnitude of the wave transfer vector, $q$, which is related to the angle of measurement, $\theta$, by the equation: $q = 4\pi \sin(\theta/2)/\lambda$. Since $q$ has inverse units of length ($Å^{-1}$), scattering in the USAXS region ($q < 0.001$ $Å^{-1}$) provides information at the micron-scale as measured by the Bonse-Hart instrument ($10^{-4}$ $Å^{-1} < q < 10^{-1}$ $Å^{-1}$). A high signal-to-noise pin-hole SAXS camera was also used to collect the scattered intensity for 0.04 $Å^{-1} < q < 1$ $Å^{-1}$ where the signal is low. Monochromatic x-rays with a wavelength of 0.59 Å (21 keV) and a beam size of 0.8 mm × 0.8 mm were used for the USAXS data collection, while a beam size of 0.2 mm × 0.2 mm was used for the pinhole SAXS data [33]. The instrument's absolute intensity calibration was verified with glassy carbon [36].

A SAXS model was formulated by collecting high-resolution, background subtracted data that combined the Bonse-Hart USAXS data with the pinhole SAXS data. As no electric field was applied for these samples, longer collection times (120 s) and both the USAXS/SAXS instrument configurations could be used to collect data for particle volume fractions of: 19, 33, 42, 54, and 63 vol%. All of these USAXS and pinhole SAXS data were reduced and combined using the IRENA [37] and NIKA [38] packages for IGOR PRO. For *in situ* experiments where an electric field was applied to the sample, time-resolved USAXS data were obtained using approximately 45–60 s collection times. The background scattering from an empty cell (without particles) with the same electrode materials was subtracted from all the slit-smeared data collected. Given that the dominant scattering features were contained within the SAXS $q$-range (0.001 $Å^{-1} < q <$ 0.04 $Å^{-1}$) and no scattering features were observed within the USAXS region, we can conclude that there are no observable micron-scale features along the substrate surface. Therefore all of the scattering data presented henceforth are referred to as SAXS data.

## III. RESULTS AND DISCUSSION

### A. Color response of EPD devices

Figure 2 shows representative images of the EPD device and its observed color response as a function of applied voltage and concentration (19–63 vol%). Here, the observed color can span a wide range of the visible spectrum, and for clarity, "OFF" refers to the 0 V state that the device returns to after the electric field is removed. Initially, in the absence of the electric field, the particle concentration determines the color of the device; as no electric field is present in these samples, the particle structure is necessarily isotropic. At low concentrations, the pigmentary color of hematite dominates, but as the particle loading is increased, the structural color in the APCs begins to mix with the pigmentary color. Similar color shifts are observed upon the application of the external

electric field. At low voltages (< 3 V), the color response is dependent on the starting particle concentration, but as the voltage is increased (up to 5 V), all concentrations eventually appear the same color. Therefore, we hypothesize that at sufficiently high applied potentials, the minimum separation distance between particles (set by the physical size of the particles) is reached.

The characteristic timescales of dynamic systems are also necessary for understanding the effect of an external stimulus. For this tunable EPD system, there are four important characteristic timescales: electrode electric double layer equilibration ($\tau_{dl} = \lambda_D L/D_i$), particle electrophoresis across the cell ($\tau_{ep} = L/\mu E$), ion diffusion across the cell ($\tau_i = L^2/D_i$), and particle diffusion across the cell ($\tau_p = L^2/D_p$), where $\lambda_D$ is the Debye length, $L$ is the electrode spacing, $\mu$ is the electrophoretic mobility, $E$ is the magnitude of the applied electric field, and $D_i$ and $D_p$ are the diffusivities of the ions and particles, respectively. Order of magnitude estimates show that $\tau_{dl} \approx 10^{-5}$ s, $\tau_{ep} \approx 10^{-2}$ s, $\tau_i \approx 10^{-1}$ s, and $\tau_p \approx 10^{2}$ s for our system [39]. The estimated $\tau_{dl}$ and $\tau_{ep}$ timescales imply that the system reaches equilibrium in a few fractions of a second as the particles deposit onto the electrode surface. Similarly, $\tau_i$ implies that the electrolyte ions will quickly diffuse away from the electrode surface once the applied bias is removed. However, $\tau_p$ implies that this quick ion diffusion is followed by a much slower particle relaxation. All of these timescales are concomitant with the instantaneous color change as well as the slow recovery behavior experimentally observed in our EPD devices.

It is important to note that an additional source of complexity is the possibility of anisotropic particle correlations near the electrode under an applied field. In this scenario, the particle mobility would have to be anisotropic over an unknown distance from the surface but isotropic in the bulk. Simulations of the system that will be presented below suggest that the particle correlations are isotropic near the electrode and that packing increases similarly in the $xy$ and $z$ directions under application of the electric field. Therefore anisotropic particle correlations are not expected in the experiment.

### B. *In situ* SAXS measurements

*In situ* SAXS measurements were performed simultaneously with the EPD experiments to gain an understanding of the real-time interparticle dynamics governing the APC system. Given the interparticle length scales of interest and the attenuation of energy through the device substrates, high-energy synchrotron radiation was used. A theoretical model was then developed for the scattering intensity, $I_p$, of a core/shell particle. Full details of the model can be found in the supplementary material [39]. In short, $I_p$ is calculated based on the well-known approach developed by Guinier *et al.* [40] for a volume distribution of spherically symmetric core/shell particles. The distribution of core size, $P(R_c, \bar{R}_c, \sigma_c)$, is assumed to be Gaussian and is parameterized by the mean core radius $\bar{R}_c$ and standard deviation $\sigma_c$. Similarly, the mean shell thickness and standard deviation are defined as $t_{\text{shell}}$ and $\sigma_p$, respectively. An effective structure factor, $S_{\text{eff}}$, was then used to account for the interparticle correlations. The simplest structure factor that incorporates the repulsive nature of the colloidal particles is the hard sphere structure factor [41]. This structure factor assumes a "hard sphere" potential between particles such that the potential energy approaches infinity at some distance from the particle center, $R_{\text{HS}}$, also known as the hard sphere radius. Thus the particles can never exist at interparticle distances less than $\eta = 2R_{\text{HS}}$ [cf. Fig 4(b)]. Finally, given its validity for narrow size distributions of particles with similar interactions, $S_{\text{eff}}$ was calculated using the decoupling approximation [42]. The resulting particle scattering intensity is given by

$$\begin{aligned} I_p(q, f_{\text{HS}}, \nu_{\text{HS}}, \bar{R}_c, \sigma_c, \sigma_p, t_{\text{shell}}, K) \\ = K S_{\text{eff}}(q, f_{\text{HS}}, \nu_{\text{HS}}, \bar{R}_c, \sigma_c, \sigma_p, t_{\text{shell}}) \\ \sum I_{cs}(q, R_c, \sigma_c, \sigma_p, t_{\text{shell}}) P(R_c, \bar{R}_c, \sigma_c) \Delta R_c + b, \end{aligned} \quad (2)$$

where $K$ is a scaling constant, $I_{cs}(q, R_c, t_{\text{shell}}, \sigma_p, \sigma_c)$ is the scattered intensity from a core/shell particle, $\nu_{\text{HS}}$ is the effective local volume fraction, and $b$ is a flat background intensity. The length of $R_{\text{HS}}$ is bounded by a physical constraint ($f_{\text{HS}} \leqslant 1$) such that $R_{\text{HS}}$ can never be smaller than the size of the particle itself. Equation (2) represents the theoretical small-angle scattering from individual core/shell particles and accounts for the interparticle correlations due to separate core and shell size distributions. In the absence of an applied voltage, high-resolution SAXS data were collected for samples at various concentrations and used to refine the model fit parameters in Eq. (2) (see Fig. S2 in Ref. [39]). The mean interparticle distance, $\eta$, was then extracted from the hard sphere structure factor.

It should be noted that alternative structure factors that account for the double layer interactions of charged colloids are common and could have instead been incorporated into the SAXS model [43,44]. These particular structure factors, however, contain several additional parameters (such as the local ionic strength and particle surface charge) that must either be fit or assumed. A structure factor that also accounts for the cubic hematite core shape could have similarly been used [40,45]; however, this approach also requires multiple assumptions and was shown to have minimal effect on the quality of the SAXS model fitting (see supplemental for details) [39]. Therefore, for the purpose of the SAXS model, the core/shell particles are considered be spherically symmetric and a simple hard sphere structure factor with only two fit parameters—$R_{\text{HS}}$ and $\nu_{\text{HS}}$—was employed since it required the least amount of fitted parameters.

For the EPD experiments with an applied bias, we chose two representative $Fe_2O_3/SiO_2$ particle concentrations of 42 and 54 vol% for further *in situ* SAXS studies. Based on the scattering model, the mean particle radius ($\bar{R}_p$) and shell thickness ($\bar{s}$) from the average of each *in situ* test were $\bar{R}_p = 77.5 \pm 1.0$ nm and $\bar{s} = 53.2 \pm 1.0$ nm, respectively, and closely agree with the SEM results (Fig. S1) [39]. Figure 3 shows the corresponding x-ray scattering intensities for the 42 vol% sample as a function of $q$ at each applied voltage (see supplemental for 54 vol% data) [39]. In both the 42 vol% (Fig. 3) and 54 vol% (Fig. S6) cases, a distinct peak in scattering intensity can be seen near $q = 0.004$ Å$^{-1}$. This scattering peak corresponds to the average particle-particle separation distance (on the order of hundreds of nanometers) that ultimately governs the observed color of the devices. The

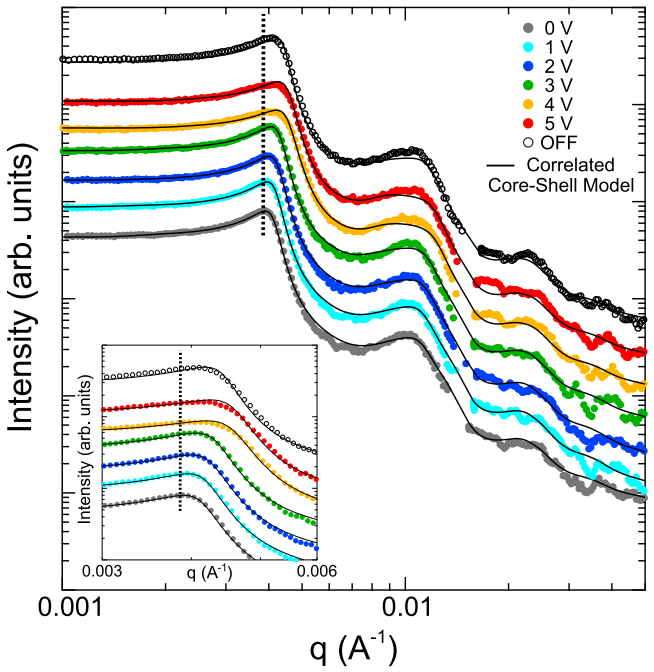


FIG. 3. Slit-smeared SAXS Intensity vs $q$ plots with associated fits for 42 vol% samples. Data for each voltage are offset on the $y$ axis for better visualization. The vertical dashed line highlights the scattering peak shift near $q = 0.004$ Å$^{-1}$. (inset) Magnified view of intensity peak shift at $0.003 < q$ (Å$^{-1}$) $< 0.006$. The final OFF scan was completed ∼30 s after removal of the electric field.

core/shell scattering model is then fit to this $q$-peak in order to determine the characteristic hard sphere radius ($R_{HS}$). The hard sphere radius does not represent the physical radius of the particle, but rather the mean radius of the sphere that corresponds to the excluded volume around a particle [Fig. 4(b)]. As the voltage is increased, the low-$q$ peak begins to shift toward higher $q$ values (i.e., smaller separation distances). Once the applied bias is removed (OFF state) the peak shifts back to lower $q$ values, and particles relax toward their initial state. Continued relaxation is observed over the next several minutes (not shown).

From the scattering data and SAXS model fits in Figs. 3 and S6, the corresponding $R_{HS}$ and $\bar{R}_p$ can be extracted as a function of the applied voltage. The respective results for both the 42 and 54 vol% samples are plotted in Fig. 4(a). As voltage increases, the hard sphere radius monotonically decreases until 4 V where it plateaus. At these relatively high potentials, $R_{HS}$ approaches $\bar{R}_p$ which suggests that the particles are tightly packed. Additional increases in the applied potential, therefore, have a negligible effect on the interparticle spacing and do not yield any further observable color change. This result supports the hypothesis that above a threshold voltage, the minimum interparticle distance is ultimately set by the physical size of the particles.

### C. Mesoscale modeling of particle dynamics

Considering the interparticle distance is directly calculated from the SAXS measurements, a multiparticle mesoscale model was developed to understand the changes in particle spacing in response to an applied voltage. This mesoscale model is based on numerical EPD simulations developed by Giera *et al.* [5], which leverages the open-source molecular dynamics software LAMMPS [46]. Unlike previous iterations of this model that required supercomputing resources [4,5], the simulations for this work were performed using a standard desktop computer. In order to perform the simulations, a model of the pairwise interaction energies between the particles is necessary. DLVO theory is commonly used to describe such pairwise interaction energies [47]. Here, electrolyte ions in solution rearrange to form electric double layers near the charged surface of a particle, thus screening the surface charge—parameterized by the zeta potential $\zeta_p$—over

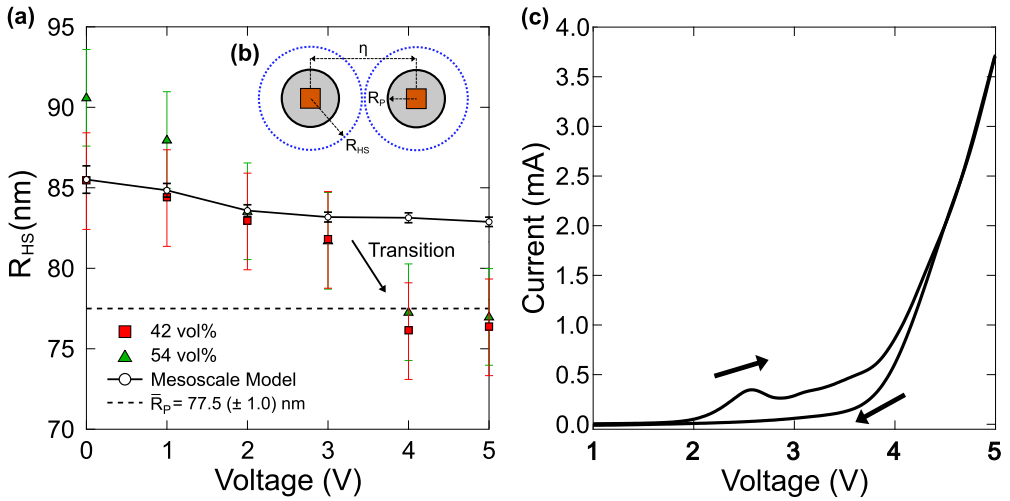


FIG. 4. (a) Calculated hard sphere radius ($R_{HS}$) vs voltage for 42 vol% (■) and 54 vol% (▲) concentrations as well as the mesoscale simulation prediction (○). Above 3 V, the measured $R_{HS}$ approaches $\bar{R}_p$ (dashed line). Vertical error bars result from spatial variability within samples (see supplemental). (b) Diagram depicting the interparticle dimensions. (c) Cyclic voltammogram of 54 vol% $Fe_2O_3/SiO_2$ core/shell particles in propylene carbonate. At greater than 3.5 V, a sharp increase in the current is observed corresponding to the onset of propylene carbonate oxidation reactions. Arrows represent direction of voltage sweep.

a characteristic length scale known as the Debye length $\lambda_D$. Neither $\zeta_p$ nor $\lambda_D$ are directly measurable in the experiment. However, it is possible to determine $\zeta_p$ from a measurement of the electrophoretic particle mobility as long as $\lambda_D$ is known. Given $\lambda_D$ is not known in our experiment, it is treated as a free parameter in the DLVO model. Here, $\lambda_D$ was chosen to be 3.6 nm, which leads to $\zeta_p = -32$ mV and allows the model to match the experimental value of $R_{\mathrm{HS}}$ for the 0 V case. This Debye length corresponds to a millimolar ionic strength and is reasonable given the solubilities of various salts in propylene carbonate [48]. A separate estimation of the Debye length, based on the solution conductivity, produced a value on the same order of magnitude as the above DLVO prediction, corroborating the fitted $\lambda_D$ value. In addition to the electrostatic potential, DLVO theory also accounts for the van der Waals attraction and steric repulsion between colloids. Please refer to the supplemental information for a more detailed discussion of the DLVO potential used in the mesoscale model [39]. Apart from DLVO interactions, colloids also interact with the surrounding suspension, giving rise to Brownian motion as well as lubrication forces at closer inter-colloidal separation distances. During EPD, particles also experience body forces due to an externally applied electric field toward an electrode (or wall) that imparts a steric-based repulsive force in the opposite direction. All of these interactions are accounted for in the mesoscale model by the total interaction potential energy $\phi_{\mathrm{tot}}$ given as

$$\phi_{\mathrm{tot}}(\mathbf{r}; z) = \phi_{\mathrm{DLVO}}(\mathbf{r}) + \phi_{\mathrm{sus}}(\mathbf{r}) + \phi_{\mathrm{field}}(z) + \phi_{\mathrm{wall}}(z), \qquad (3)$$

where $\phi_{\mathrm{DLVO}}$ is the DLVO interaction potential detailed above, $\phi_{\mathrm{sus}}$ is the colloid-solvent interaction potential—both of which act as a function of pairwise distance between particles $\mathbf{r}$—while $\phi_{\mathrm{field}}$ and $\phi_{\mathrm{wall}}$ account for particle-electric field and particle-wall interactions at distance $z$ from the wall, respectively (see Giera *et al.* [5] for details on the derivation of these potentials). Input parameters of the mesoscale model solely include measurable colloidal suspension properties such as the particle radius $\bar{R}_p$, $\zeta_p$, $\lambda_D$, etc., which fully specify the terms in Eq. (3). Since the model is formulated within in the molecular dynamics framework, colloidal trajectories are determined by computing Newton's equations of motion at discretized time steps of 0.5 ns. First, we initialize a simulation cell with 400 deposited particles. Then, we equilibrate the system for 10 ms at the desired electric field strength, and finally, we collect and analyze the positional data with a sampling frequency of 0.05 ms for an additional 10 ms. For each of the 200 sampled equilibrated particle configurations, we use the OVITO PYTHON package [49] to generate radial distribution functions whose average first peak location corresponds directly to $2R_{\mathrm{HS}}$. Figure 4(a) shows the time-averaged prediction of $R_{\mathrm{HS}}$ from the simulation with error bars representing the standard deviation. There is quantitative agreement between the experiment and simulation up to an applied voltage of 3 V. After 3 V, the particles appear to rapidly transition such that $R_{\mathrm{HS}} \sim \bar{R}_p$, that is, the particle surfaces are close to touching. We hypothesize this high voltage deviation is due to an increase in the local ionic strength from electrochemical reactions near the electrode surface. It should be noted that there is a clear distinction between the "local" and the overall "bulk" ionic strength. An increase in the local ionic strength will lead to additional surface charge screening and, in turn, decrease the Debye length in the region near the electrode allowing the particles to approach each other. This hypothesis is supported by the fact that cell current increases sharply after 3.5 V as can be seen from cyclic voltammetry, Fig. 4(c). These mechanisms are not included in the mesoscale model but are considered to be responsible for the observed discrepancy at higher applied potentials.

It is well known that such electrochemical reactions occur near 4 V in propylene carbonate including the oxidation of propylene carbonate (independent of the identity of the electrolyte salt) which generates $CO_2$ gas as well as $CO_3^{2-}$ and other radical ions [50–52]. These radical ions could then interact with the surface of the particles to form a transient propylene glycol film leading to additional steric stabilization of the particles [50]. Even when the particles are in close proximity, this film could prevent irreversible adsorption or aggregation. Further increases in the applied potential would then have little effect on the observed color change. Once the applied voltage is removed, the generated ions will diffuse away from the electrode surface and the particles will resuspend. After resuspension, the device would return to its original color, as observed experimentally.

### D. UV-Vis reflectance measurements

Both the SAXS and mesoscale simulation results show that small changes in the particle spacing correlate to significant differences in the device color. To quantify these color changes, UV-Vis spectroscopy was used to measure the reflectance spectra as a function of the applied voltage. Figure 5 shows the normalized reflectance ($\hat{R}_i$) for 42 vol% $Fe_2O_3/SiO_2$ particles (cf. Fig. S7 for 54 vol% data) [39]. From the spectra in Fig. 5(a), two separate regimes are observed. At wavelengths of $\lambda > 550$ nm, absorption due to the inherent pigmentary color of hematite is seen over all applied voltages [23]. However, below wavelengths of 550 nm, scattering due to the structural color of the core/shell particles dominates the spectrum. The wavelength of maximum scattering responsible for variations in the structural color occurs solely at positive integer multiples, $m$ [Eq. (1)]. Thus there should only be one peak within the visible wavelength range due to scattering from the particles, and this peak is the only one expected to shift in wavelength with respect to changes in the interparticle spacing. We refer to the wavelength where the maximum of this peak occurs as $\lambda_{\mathrm{max}}$.

At 0 V, the device initially exhibits two peaks in the structural reflectance region: one centered near $\lambda = 480$ nm and the other at $\lambda = 520$ nm. As the voltage is increased, the 480 nm peak increases in intensity as well as shifts toward shorter wavelengths. Comparatively, the 520 nm peak solely decreases in intensity. The structural scattering due to variations in the interparticle spacing (which is responsible for observable color changes of the device) is, therefore, attributed to the 480 nm peak. These shifts in the measured reflectance are normalized in Fig. 5(b) by subtracting out the initial (0 V) state of the device (see supplemental for details) [39]. As voltage is increased, wavelengths where $\Delta\hat{R}_i < 0$ indicate regions of increased transmittance/absorbance. Likewise,

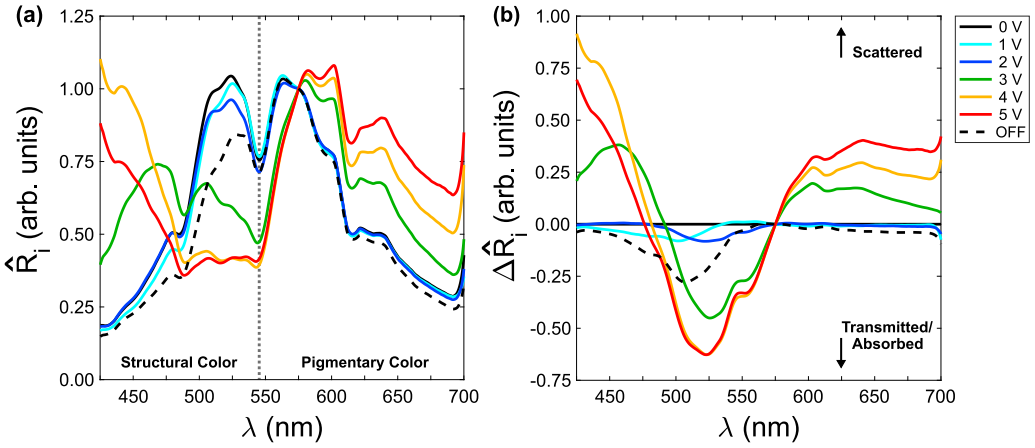


FIG. 5. (a) Normalized visible reflectance spectra for a 42 vol% concentration device. The inherent pigmentary color of iron oxide dominates at $\lambda > 550$ nm. Variations in structural color below $\lambda = 550$ nm show a blue-shift with increasing applied voltage. (b) Change in device reflectance ($\Delta\hat{R}_i$) from the initial 0 V state. $\Delta\hat{R}_i > 0$ corresponds to wavelengths of increased scattering compared to 0 V.

wavelengths where $\Delta\hat{R}_i > 0$ indicate regions of increased scattering. Light from these scattered regions combines to give the overall perceived color of the device. As a result, we are able to directly measure the mixing effects of the iron oxide pigmentary color and the tunable structural color of the particles at each voltage.

### E. Particle correlation scattering and structural color comparison

A particle correlation scattering analysis was conducted to directly relate changes in the interparticle spacing (measured with *in situ* EPD/SAXS) to the observed UV-Vis color response of the devices. Figures 6(a) and 6(b) show representative simulation snapshots of the visible light scattering from a tunable APC as a result of such particle correlations. Initially, when the device is off, the particles are loosely packed. Once a voltage is applied, a color shift occurs as the particles deposit to form a denser, more tightly packed film near the electrode.

Typically in the literature, $\lambda_{max}$ for an APC system is first measured, and then the interparticle separation distance is inferred using Eq. (1) or assumed based on FCC or some other simple packing order [27,30,31]. Using SAXS, however, we are able to first directly measure $R_{HS}$ (i.e., $\eta$) which can be used to predict $\lambda_{max}$. This predicted scattering wavelength will be referred to as $\lambda_{SAXS}$. Since these interparticle separations are measured directly, no implicit assumptions about the particle structure or morphology of the deposit are necessary. An alternative approach would be to approximate the interparticle spacing as $\eta = 2\pi/q_{max}$ [39]. While such a simple and intuitive analysis is able to capture the general shift in $\lambda_{max}$, the asymmetry and broadness of the relatively weak SAXS peak maximum cannot be reliably extracted from a single data point, and $R_{HS}$ must instead be extracted from

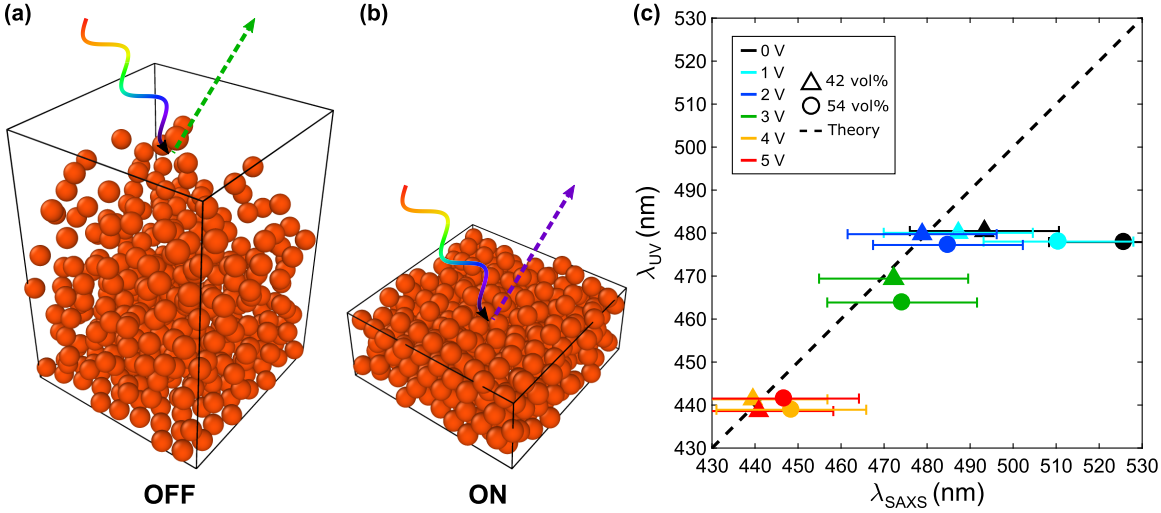


FIG. 6. Simulation snapshots from the mesoscale model depicting particle correlation scattering of visible light at (a) 0 V (OFF) and (b) 5 V (ON). Particles are more tightly packed in the ON state of the device as compared to the initial OFF state which results in an observable color shift. (c) Measured $\lambda_{UV}$ peak values compared to the predicted $\lambda_{SAXS}$ values. The 45° line denotes perfect agreement with theory. Vertical error bars result from error in Gaussian fitting of UV-Vis reflectance peaks (magnitude is smaller than the data points) while horizontal error bars result from spatial variability within samples [39].

a $q$ range. Separately, $\lambda_{max}$ can be extracted from a standard Gaussian curve fit of the structural UV-Vis peak near $\lambda = 480$ nm. This measured scattering wavelength will be referred to as $\lambda_{UV}$. Ideally, $\lambda_{SAXS} = \lambda_{UV}$. Here, the range for each Gaussian fit varies as $\lambda_{max}$ (initially located at 480 nm) shifts with increasing applied voltage, and a multi-Gaussian curve fit can be used to deconvolve the structural scattering peak.

In order to validate the direct SAXS particle correlation approach, the predicted $\lambda_{SAXS}$ values were compared to the measured $\lambda_{UV}$ values in Fig. 6(c) and showed good agreement for both the 42 and 54 vol% samples. At low applied voltages, however, $\lambda_{SAXS}$ shows some deviation from $\lambda_{UV}$. A possible explanation comes from the fact that UV-Vis is performed in reflectance, and thus is dominated by the structure near the electrode, while the SAXS measurement is performed in transmission and contains contributions from the bulk. Better agreement is observed between $\lambda_{SAXS}$ and $\lambda_{UV}$ at higher applied voltages as more particles accumulate near the electrode surface and the bulk is depleted.

It is worth noting that an alternative GISAXS sample setup [53] could be used to resolve the particle correlations normal to the electrode surface that would exclude the bulk particle contributions from the measurement. Such a sample setup, however, would significantly complicate the SAXS data analysis. Not only would scattering from the incident beam contribute to the GISAXS signal, but a distorted surface wave would also contribute. Future experiments could also employ sample-rotated SAXS (SR-SAXS) or grazing transmission SAXS (GTSAXS). These techniques have previously been employed for nanoparticle electrodeposition and could provide information—i.e., particle correlations, deposit thicknesses, and particle concentrations—normal to the electrode surface as the electrode is rotated relative to the x-ray beam path [54,55]. Such experiments would provide valuable information for understanding the fundamental behavior of our system; however, these alternative set-ups present a number of challenges (such as longer collection times over various sampling angles). Nonetheless, the transmission geometry used here is sufficient to capture the interparticle spacing that dominates the UV-Vis reflectance for a given applied voltage (Fig. 6) and can also serve as the basis for more detailed SAXS measurements in the future.

## IV. CONCLUSIONS

In summary, we developed an *in situ* experimental SAXS technique and computational model for describing the interparticle dynamics and optical properties of tunable colloidal systems. The results presented here provide a method for direct real-time measurements of the average separation distance between particles in such a system. The x-ray scattering data were fit to a core/shell particle model, and the average hard sphere radius was calculated as a function of the voltage. Finally, UV-Vis reflectance spectroscopy was used to measure the color shift of the device with respect to applied electric field and this shift is in agreement with that expected from SAXS measurements.

While the computational model quantitatively agrees with the experiments at low applied voltages, it significantly overpredicts the interparticle spacing at high voltages. We attribute this discrepancy to electrochemistry occurring at the electrode changing the local chemical environment near the deposit which is supported by the fact that electric current through the cell increases dramatically at high voltage. Further study is required to characterize the changes in chemistry that are occurring and properly account for the effects in the computational model.

The experimental and theoretical results presented here can be broadly applied to many dynamic colloidal systems. This *in situ* SAXS technique can be used to describe transient, field dependent microstructural changes in colloidal systems that lead to other observable properties (e.g., transparency, chemical conversion, mechanical strain, thermal conductivity, etc.). Although the synchrotron x-ray intensities used here are ~103 times higher than current laboratory-based x-ray sources, a lower intensity, more readily accessible x-ray source could be sufficient to resolve the lower $q$ peak intensities associated with length scales on the order of 100 nm (i.e., $R_{HS}$). Laboratory-based x-ray scattering approaches and/or quantitative color difference analyses would open the possibility for everyday bench-top characterizations of other tunable systems. Results from this work could also be used to further validate existing colloidal crystallization/EPD models and simulations and provide a better fundamental understanding of tunable, color changing APC systems.

## ACKNOWLEDGMENTS

This work was performed under the auspices of the US Department of Energy by Lawrence Livermore National Laboratory under Contract No. DE-AC52-07NA27344 LLNL-JRNL-750717. This research also used resources of the Advanced Photon Source (APS Sector 9-ID-C), a US Department of Energy (DOE) Office of Science User Facility operated for the DOE Office of Science by Argonne National Laboratory under Contract No. DE-AC02-06CH11357. We would also like to acknowledge LLNL researchers Caitlyn Cook, Alyssa Troksa, and Tyler Fears for their added intellectual contributions and efforts.

[1] P. Sarkar and P. S. Nicholson, J. Am. Ceram. Soc. **79**, 1987 (1996).
[2] L. Besra and M. Liu, Prog. Mater. Sci. **52**, 1 (2007).
[3] B. Ferrari and R. Moreno, J. Eur. Ceram. Soc. **30**, 1069 (2010).
[4] B. Giera, L. A. Zepeda-Ruiz, A. J. Pascall, J. D. Kuntz, C. M. Spadaccini, and T. H. Weisgraber, J. Electrochem. Soc. **162**, D3030 (2015).
[5] B. Giera, L. A. Zepeda-Ruiz, A. J. Pascall, and T. H. Weisgraber, Langmuir **33**, 652 (2017).
[6] O. Van der Biest and L. J. Vandeperre, Annu. Rev. Mater. Sci. **29**, 327 (1999).
[7] P. Sarkar, D. De, and H. Rho, J. Mater. Sci. Lett. **39**, 819 (2004).
[8] G. Anné, K. Vanmeensel, J. Vleugels, and O. Van der Biest, Key Eng. Mater. **314**, 213 (2006).

[9] D. W. Templeton, T. J. Gorsich, and T. J. Holmquist, *Computational Study of a Functionally Graded Ceramic-Metallic Armor* (Tacom Research Development and Engineering Center Warren, MI, 2006).

[10] S. Novak and A. Iveković, J. Nucl. Mater. **427**, 110 (2012).

[11] K. T. Sullivan, M. A. Worsley, J. D. Kuntz, and A. E. Gash, Combust. Flame **159**, 2210 (2012).

[12] W. Shan, Y. Zhang, W. Yang, C. Ke, Z. Gao, Y. Ye, and Y. Tang, Microporous Mesoporous Mater. **69**, 35 (2004).

[13] M. Matsuda, M. Hashimoto, C. Matsunaga, T. S. Suzuki, Y. Sakka, and T. Uchikoshi, J. Eur. Ceram. Soc. **36**, 4077 (2016).

[14] T. Kitabatake, T. Uchikoshi, F. Munakata, Y. Sakka, and N. Hirosaki, J. Ceram. Soc. Jpn. **118**, 1 (2010).

[15] M. Diba, D. W. H. Fam, A. R. Boccaccini, and M. S. P. Shaffer, Prog. Mater. Sci. **82**, 83 (2016).

[16] A. R. Boccaccini, S. Keim, R. Ma, Y. Li, and I. Zhitomirsky, J. R. Soc., Interface **7**, S581 (2010).

[17] K. Moritz and T. Moritz, J. Eur. Ceram. Soc., **30**, 1203 (2010).

[18] S. Fiorilli, F. Baino, V. Cauda, M. Crepaldi, C. Vitale-Brovarone, D. Demarchi, and B. Onida, J. Mater. Sci. Lett.: Mater. Med. **26**, 21 (2015).

[19] J. D. Forster, H. Noh, S. F. Liew, V. Saranathan, C. F. Schreck, L. Yang, J.-G. Park, R. O. Prum, S. G. J. Mochrie, C. S. O'Hern, H. Cao, and E. R. Dufresne, Adv. Mater. **22**, 2939 (2010).

[20] A. T. Heitsch, R. N. Patel, B. W. Goodfellow, D.-M. Smilgies, and B. A. Korgel, J. Phys. Chem. C **114**, 14427 (2010).

[21] S. F. Liew, J. Forster, H. Noh, C. F. Schreck, V. Saranathan, X. Lu, L. Yang, R. O. Prum, C. S. O'Hern, E. R. Dufresne, and H. Cao, Opt. Express **19**, 8208 (2011).

[22] A. J. Krejci, K. G. Yager, C. Ruggiero, and J. H. Dickerson, Nanoscale **6**, 4047 (2014).

[23] J. Han, E. Lee, J. K. Dudoff, M. Bagge-Hansen, J. R. I. Lee, A. J. Pascall, J. D. Kuntz, T. M. Willey, M. A. Worsley, and T. Y.-J. Han, Adv. Opt. Mater. **5**, 1600838 (2017).

[24] Y. Yu, D. Yu, B. Sadigh, and C. A. Orme, Nat. Commun. **9**, 4211 (2018).

[25] Y. Lu, H. Xia, G. Zhang, and C. Wu, J. Mater. Chem. **19**, 5952 (2009).

[26] I. Lee, D. Kim, J. Kal, H. Baek, D. Kwak, D. Go, E. Kim, C. Kang, J. Chung, Y. Jang, S. Ji, J. Joo, and Y. Kang, Adv. Mater. **22**, 4973 (2010).

[27] T. S. Shim, S.-H. Kim, J. Y. Sim, J.-M. Lim, and S.-M. Yang, Adv. Mater. **22**, 4494 (2010).

[28] F. Liu, B. Dong, and X. Liu, in *Optical Devices in Communication and Computation*, edited by P. Xi (IntechOpen, London, 2012).

[29] L. Shi, Y. Zhang, B. Dong, T. Zhan, X. Liu, and J. Zi, Adv. Mater. **25**, 5314 (2013).

[30] L. Nucara, F. Greco, and V. Mattoli, J. Mater. Chem. C **3**, 8449 (2015).

[31] Y. Takeoka, J. Mater. Chem. C **1**, 6059 (2013).

[32] B. Giera, S. Bukosky, E. Lee, M. Freyman, J. Han, T. Y.-J. Han, M. A. Worsley, J. D. Kuntz, and A. J. Pascall, ECS Trans. **82**, 59 (2018).

[33] J. Ilavsky, A. J. Allen, L. E. Levine, F. Zhang, P. R. Jemian, and G. G. Long, J. Appl. Crystallogr. **45**, 1318 (2012).

[34] S. C. Bukosky and W. D. Ristenpart, Langmuir **31**, 9742 (2015).

[35] S. C. Bukosky, S. M. H. Hashemi Amrei, S. P. Rader, J. Mora, G. H. Miller, and W. D. Ristenpart, Langmuir **35**, 6971 (2019).

[36] F. Zhang, J. Ilavsky, G. G. Long, J. P. G. Quintana, A. J. Allen, and P. R. Jemian, Metall. Mater. Trans. A **41**, 1151 (2010).

[37] J. Ilavsky and P. R. Jemian, J. Appl. Crystallogr. **42**, 347 (2009).

[38] J. Ilavsky, J. Appl. Crystallogr. **45**, 324 (2012).

[39] See Supplemental Material at http://link.aps.org/supplemental/10.1103/PhysRevMaterials.4.075802 for further description of the SAXS and UV-Vis experiments/analytical modeling as well as full details on the theoretical modeling.

[40] A. Guinier and G. Fournet, *Small-Angle Scattering of X-Rays* (Wiley, New York, 1955).

[41] N. W. Ashcroft and J. Lekner, Phys. Rev. **145**, 83 (1966).

[42] M. Kotlarchyk and S. Chen, J. Chem. Phys. **79**, 2461 (1983).

[43] J. B. Hayter and J. Penfold, Mol. Phys. **42**, 109 (1981).

[44] J.-P. Hansen and J. B. Hayter, Mol. Phys. **46**, 651 (1982).

[45] O. Glatter and O. Kratky, *Small Angle X-Ray Scattering* (Academic Press, London; New York, 1982).

[46] S. Plimpton, J. Comput. Phys. **117**, 1 (1995).

[47] J. N. Israelachvili, *Intermolecular and Surface Forces* (Elsevier Science, Amsterdam, 2011).

[48] P. K. Muhuri, S. K. Ghosh, and D. K. Hazra, J. Chem. Eng. Data **38**, 242 (1993).

[49] A. Stukowski, Modell. Simul. Mater. Sci. Eng. **18**, 015012 (2010).

[50] B. Rasch, E. Cattaneo, P. Novak, and W. Vielstich, Electrochim. Acta **36**, 1397 (1991).

[51] K. Kanamura, T. Umegaki, M. Ohashi, S. Toriyama, S. Shiraishi, and Z.-i. Takehara, Electrochim. Acta **47**, 433 (2001).

[52] L. Xing, C. Wang, W. Li, M. Xu, X. Meng, and S. Zhao, J. Phys. Chem. B **113**, 5181 (2009).

[53] X. Lu, K. G. Yager, D. Johnston, C. T. Black, and B. M. Ocko, J. Appl. Crystallogr. **46**, 165 (2013).

[54] J. A. Hammons, J. Ustarroz, T. Muselle, A. A. J. Torriero, H. Terryn, K. Suthar, and J. Ilavsky, J. Phys. Chem. C **120**, 1534 (2016).

[55] J. A. Hammons, F. Zhang, and J. Ilavsky, J. Colloid Interface Sci. **520**, 81 (2018).